Impact response of semicylindrical woven composite shells: The effect of stacking sequence

L.M. Ferreira [a,b,*], M. Muñoz-Reja [a,b], P.N.B. Reis [c]

[a] *Grupo de Elasticidad y Resistencia de Materiales, Escuela Técnica Superior de Ingeniería, Universidad de Sevilla, Camino Descubrimientos, S/N 41092 Sevilla, Spain*
[b] *Escuela Politécnica Superior, Universidad de Sevilla, C/ Virgen de África, 7, Sevilla, 41011, Spain*
[c] *University of Coimbra, CEMMPRE, ARISE, Department of Mechanical Engineering, 3030-194 Coimbra, Portugal*

ABSTRACT

The existing literature extensively explores the influence of stacking sequences on symmetric flat laminates subjected to low-velocity impacts. However, this is not true in the case of curved laminates. Therefore, the main goal of this study is to analyse the effect of stacking sequences on the impact response of semicylindrical woven composite shells. For this purpose laminates with $[0]_8$, $[45]_8$, $[+15,-15]_{2S}$, $[+22.5,-22.5]_{2S}$, and $[+30,-30]_{2S}$, were considered in order to evaluate the impact response of layer orientations. Additionally, laminates with $[0_2, 45_2]_S$, $[0,45]_{2S}$, $[0,45_2, 0]_S$, and $[45_2, 0_2]_S$ were employed to analyse the effects of changing the positioning of the layers in relation to the laminate mid-plane. The FE model was validated with the experimental results obtained for $[0]_8$ laminates, where good numerical–experimental correlation was obtained. The findings suggest that an increase in impact bending stiffness (IBS) leads to a rise in maximum force, accompanied by a decrease in maximum displacement, contact time, and dissipated energy. The primary mechanism responsible for dissipating the majority of impact energy is intralaminar damage, followed by delaminations and friction. Importantly, changing the layer positions has a significant impact on how each layer within the semicylindrical quasi-isotropic composite shell distributes and dissipates energy during the impact event.

1. Introduction

Composite materials are increasingly replacing traditional materials, such as metals, due to their intrinsic properties. However, the low resistance across the thickness compromises their application in many cases, even with all the benefits mentioned. According to the literature, this sensitivity is especially important when it comes to impact loads, which might happen during service or maintenance conditions and result in damage that is very difficult to detect visually [1–3].

In this context, it is not surprising that literature presents numerous studies on their impact response. However, most of them focus on symmetrical laminates because this configuration eliminates the in-plane and out-of-plane interactions responsible for distortions during the curing process. Consequently, there is an increase in internal stress levels and a corresponding decrease in load capacity [4–6]. In the specific case of low-velocity impact, numerical and experimental studies available in the bibliography highlight the influence of the stacking sequence on the parameters that characterise the impact response [7–14]. For example, both the maximum load and displacement, energy

absorption capacity, and impact bending stiffness (directly related to the damage) depend on the balanced lamina position about the mid-plane in the laminate but are independent of the number of angles of mismatching interfaces. Furthermore, by affecting the previously mentioned parameters, the onset and propagation of interlaminar and intralaminar damage are also affected, with the latter (intralaminar damage) being directly responsible for the energy absorption and residual displacement in the damaged region [7–10]. The same can be replicated for the effect on the response to multiple impacts, where the grouping of layers promotes an increase in bending stiffness and stress concentration at the interfaces and, consequently, different damage patterns due to larger delaminations. Therefore, ply grouping reduces the damage resistance in laminates and, in this context, the stacking sequence should be considered at the design stage to improve impact resistance [11–14].

However, most of the studies published in the literature are on flat plates, and very few address the effect of the stacking sequence on the

---

impact performance of semi-cylindrical woven composites. Given that the use of composite materials in advanced structures is increasing and, for design reasons, cylindrical shells are also increasingly in demand, it is important to know their mechanical performance, especially their response to low-velocity impact. From the available studies [15–18], it is already recognised that in composite shells the damages start at the top ply and propagate into the lower layers, however, the damage is minimal when the bending stiffness is equal in the axial and circumferential directions. The damage can be characterised by fibre fractures and some delaminations around the broken fibres, in the region where the impactor contacts the composite but, depending on the fibre type, it can be more severe in the lower layers due to the predominance of tensile stresses over the compressive ones (occurred in the upper layers). Furthermore, fibre fractures and delaminations are the main failure mechanisms that trigger intralaminar damage, which is approximately five times more important than the other energy dissipation modes [15,17,18]. Regarding the thickness effect on the impact response of semi-cylindrical woven composites, literature reports that for thicker curved shells the damage is more severe along the thickness, while in thinner ones is more extensive. Moreover, impact damage becomes more localised with increasing thickness because the energy is dissipated by more interfaces, while the stacking sequence affects the damage size because more interfaces between different plies can lead to a higher impact velocity threshold and smaller damage size [15–17].

Therefore, because the stacking sequence and the number of interfaces determine the severity of the damage, the design phase should immediately include an optimisation process. For this purpose, this study aims to provide a numerical tool to help designers in this task, where the stacking sequence will be evaluated to assess its influence on the damage after impact in semicylindrical woven composite shells. To the best of the authors' knowledge, this study is unprecedented and focuses on symmetrical sequences due to the significant advantages associated with them. Sequences with $[0]_8$, $[45]_8$, $[+15,-15]_{2S}$, $[+22.5,-22.5]_{2S}$, and $[+30,-30]_{2S}$ were generated to study the effect of the layer orientations. Additionally, sequences with $[0_2,45_2]_S$, $[0,45]_{2S}$, $[0,45_2,0]_S$, and $[45_2,0_2]_S$ are used to analyse the effect of changing the positioning of the layers in relation to the laminate midplane. Finally, it is also determined the energy dissipation mechanisms that take place during low-velocity impact events and anticipate and evaluate the intralaminar and interlaminar damage modes.

2. Experimental procedure

Composite semicylindrical shells were fabricated through resin transfer moulding, with an internal radius of 50 mm, a length of 100 mm, and an averaged thickness of 2.53 mm. The structure of these shells consists of eight layers of woven carbon fibre fabric (160 g/cm^2, plain-weave), sourced from Composite Materials Italy (CIT), intertwined with SR 1500 epoxy resin and SD2503 hardener, both provided by Sicomin (Châteauneuf-les-Martigues, France). The positioning of the eight bi-directional (0°/90°) layers was performed via hand lay-up, maintaining their alignment with the direction of the semicylindrical shell longitudinal axis and identical for all layers. For simplification, this layup configuration is denoted as $[0]_8$.

The assurance of consistent fibre volume fraction, uniform thickness, and the elimination of any entrapped air bubbles was upheld by subjecting the laminates to a 24-h vacuum bagging process at 0.8 bar immediately after impregnation. A subsequent post-curing procedure was executed in accordance with the manufacturer's guidelines, involving an exposure of 8 h at 60 °C.

Subsequently, low-velocity impact responses were assessed using an IMATEK-IM10 (Old Knebworth, United Kingdom) drop weight impact testing machine. An impactor possessing a diameter of 10 mm and a mass of 2.826 kg, corresponding to an impact energy of 5 J, was employed. These conditions were chosen to induce discernible damage in the specimens while avoiding perforation. As depicted in Fig. 1,

the impact point was situated at the centre of the specimens, which were simply supported on both straight edges and left free on the curved edges. The impact energy produced by gravity is altered by changing the drop height. More information about the equipment and data acquisition system can be found in [19,20] but, basically, the impact force was measured with a 32,000 point piezoelectric load cell, and the deflection was obtained by double integrating the acceleration versus time curve.

The experimental tests were carried out in accordance with the ASTM D7136 [21], at room temperature and, as suggested by the standard, a minimum of five specimens were used to guarantee the repeatability of the experiment. Subsequently, the average experimental curve will be used for comparison with the numerical one. More detailed information on the materials used, the manufacturing process, and the experimental test procedure can be found in [22,23].

3. Numerical model

The subsequent section provides a succinct overview of the intralaminar, and interlaminar damage models that were integrated into the FE models used in this study. These models facilitate the computational simulations of low-velocity impact tests, and were defined based upon the experimental assessments conducted in [22], alongside the numerical investigation performed in [24,25], utilising the ABAQUS/Explicit FE software [26].

Additionally, the geometric parameters and imposed boundary conditions of both the specimen and the impactor are presented. The discretisation strategy for the FE mesh is detailed, encompassing the specification of element types employed, and the definitions of contact interactions between all modelled components. The correct establishment of these parameters, founded on the experimental procedure, serve for the subsequent validation of the generated FE model.

3.1. Damage models

To accurately capture the damage that occurs at the intralaminar level of the woven fabric composite shells, it is essential to employ a continuum damage mechanics model (CDM) specifically designed for fabric-reinforced composites. In this specific case, the model was implemented in ABAQUS/Explicit FE software [26] through the utilisation of the integrated VUMAT subroutine ABQ_PLY_FABRIC [27], devised by Johnson [28], which is rooted in the Ladeveze and LeDantec damage model [29]. This VUMAT subroutine exhibits compatibility solely with plane-stress elements, and characterises each woven fabric-reinforced lamina as an orthotropic elastic material. The material integrity is subject to degradation in stiffness attributable to the occurrence of fibre failure, matrix cracking, and plastic deformation during shear-loading conditions. It employs the maximum stress failure criterion to ascertain the initiation of damage within the fibres, while employing a damage evolution model based on fracture energies to govern the ensuing reduction in stiffness. Notice that this formulation was successfully employed by the authors to numerically study the low-velocity impact response of E-glass/Polyester woven fabric reinforced composites [24,25]. These studies revealed that the maximum load, maximum displacement, and contact time are negligibly affected by the choice of FE mesh discretisation and of the cohesive stiffness. However, to accurately compute delamination, their correct definition is of upmost importance. Additionally, the findings indicate that only the normal cohesive strength affects the maximum impact force and delamination predictions.

The elastic stress–strain relationship for the degraded orthotropic material is defined as follows,

$$\begin{bmatrix} \frac{S_1}{(1-d_1)} & S_{12} & 0 \\ S_{21} & \frac{S_2}{(1-d_2)} & 0 \\ 0 & 0 & \frac{S_6}{(1-d_{12})} \end{bmatrix} = \begin{bmatrix} \frac{S_1}{(1-d_1)} & S_{12} & 0 \\ S_{21} & \frac{S_2}{(1-d_2)} & 0 \\ 0 & 0 & \frac{S_6}{(1-d_{12})} \end{bmatrix} \sigma \qquad (1)$$
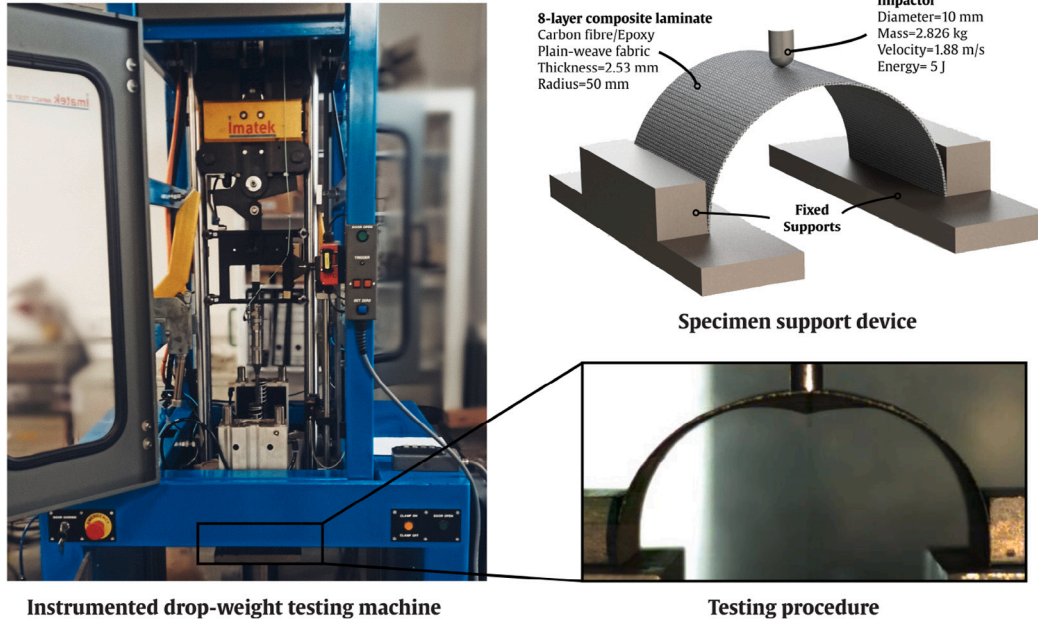
Fig. 1. Representation of the experimental testing procedure.

where, S_{ij} represents the components of the compliance matrix pertaining to the orthotropic material, σ signifies the nominal Cauchy stress tensor and ε stands for the elastic strain tensor. Additionally, d_α represents the damage variables of the model with $\alpha = \{1+, 1-, 2+, 2-, 12\}$, since the model differentiates between tensile and compressive failure. These damage variables take values $0 \leq d_\alpha < 1$ representing modulus reductions under different loading conditions due to microdamage in the material. Note that, the damage variable d_1 and d_2 are associated with the damage along the first and second directions, respectively, whereas d_{12} pertains to matrix micro-cracking as a consequence of shear deformation.

The elastic domain, determined at any specific instance, is computed based on the activation functions of damage, denoted as F_α and formulated as

$$F_\alpha = \frac{\tilde{\sigma}_\alpha}{X_\alpha} - r_\alpha \leq 0 \quad \text{with} \quad \alpha = \{1+, 1-, 2+, 2-, 12\} \tag{2}$$

where $\tilde{\sigma}_\alpha$ stand for the effective stresses defined as $\tilde{\sigma}_{1+} = \frac{\langle\sigma_{11}\rangle}{(1-d_{1+})}$, $\tilde{\sigma}_{1-} = \frac{\langle-\sigma_{11}\rangle}{(1-d_{1-})}$, $\tilde{\sigma}_{2+} = \frac{\langle\sigma_{22}\rangle}{(1-d_{2+})}$, $\tilde{\sigma}_{2-} = \frac{\langle-\sigma_{22}\rangle}{(1-d_{2-})}$ and $\tilde{\sigma}_{12} = \frac{\sigma_{12}}{(1-d_{12})}$; X_α are the strengths; and r_α signifies the damage thresholds, initially set to a value of 1.

Once the damage onset is achieved, specifically when $\frac{\tilde{\sigma}_\alpha}{X_\alpha} = 1$, the progression of the damage coefficients d_1 and d_2, pertaining to tensile and compressive loading, is determined utilising the following expression

$$d_\alpha = 1 - \frac{1}{r_\alpha} e^{-A_\alpha(r_\alpha-1)} \quad \text{where} \quad \dot{d}_\alpha \geq 0 \tag{3}$$

$$\text{with} \quad A_\alpha = \frac{2g_0^\alpha L_{ch}}{G_f^\alpha - g_0^\alpha L_{ch}} \quad \text{and} \quad \alpha = \{1+, 1-, 2+, 2-\}$$

where L_{ch} is the characteristic length of the plate; G_f^α is the fracture energy per unit area under tensile/compressive loading, and $g_0^\alpha = \frac{X_\alpha^2}{2E_\alpha}$ is the elastic energy density per unit volume at the initial damage point.

While the evolution of the damage coefficient d_{12} in relation to the shear load is described by this expression

$$d_{12} = \min\{\alpha_{12} \ln(r_{12}), \, d_{12}^{max}\} \tag{4}$$

Table 1
Intralaminar properties defined for the woven-fabric reinforced composite laminas [30].

Property	Symbol	Units	Value
Density	ρ	kg/m^3	1600
Stiffness properties	$E_1^{+,-} = E_2^{+,-}$	GPa	69
	G_{12}	GPa	7.1
	$v_{12}^{+,-}$	–	0.04
Strength properties	$X_1^+ = X_2^+$	MPa	640
	$X_1^- = X_2^-$	MPa	540
	S_{12}	MPa	180

Herein, $r_{1,2}$ and r_{12} denote the damage thresholds associated with tensile/compressive and shear loading, respectively. The terms $G_f^{1,2}$ represent the fracture energies per unit area, while $g_0^{1,2}$ signifies the elastic energy density at the point of damage initiation. Additionally, L_{ch} pertains to the characteristic length of the element and α_{12} is a parameter pertaining to shear damage.

The VUMAT subroutine employs the yield and hardening functions, expressed as Eqs. (5) and (6), respectively, to determine the plasticity response of the matrix material.

$$F_{pl} = |\tilde{\sigma}_{12}| - \tilde{\sigma}_0(\bar{\varepsilon}^{pl}) \leq 0 \tag{5}$$

$$\tilde{\sigma}_0(\bar{\varepsilon}^{pl}) = \tilde{\sigma}_{y0} + C(\bar{\varepsilon}^{pl})^p \tag{6}$$

Here, $\tilde{\sigma}_{12}$ signifies the effective shear stress, while $\tilde{\sigma}_{y0}$ denotes the initial effective shear stress. Additionally, $\bar{\varepsilon}^{pl}$ represents the plastic strain resulting from shear deformation. The hardening function's coefficient and the exponentiation term are denoted as C and p, respectively.

The fundamental intralaminar material properties were extracted from [30] and are presented in Table 1.

Within this context of the employed CDM, the fracture energy release rate values, $G_f^{1,2}$, are crucial for the accurate prediction of damage progression, and therefore, to obtain valid numerical predictions of the low-velocity impact response of the composite laminate shell. However, it is important to note that establishing these intralaminar material
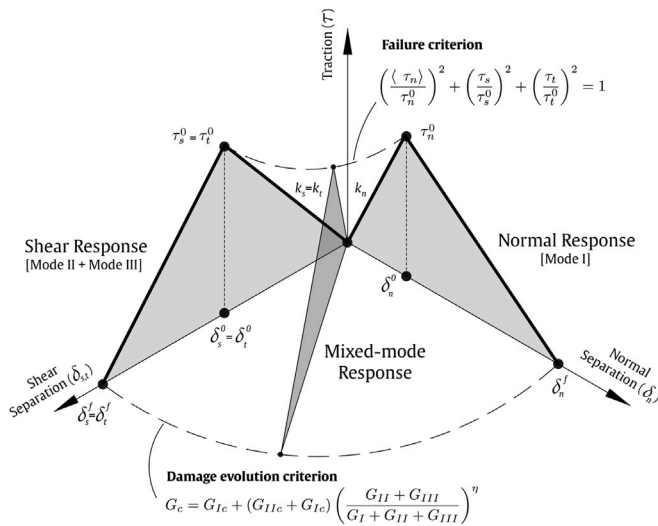
Fig. 2. Bilinear traction–separation response of the cohesive surfaces [25].

Table 2
Interlaminar properties defined for the composite shell interfaces.

Property	Symbol	Units	Value
Stiffness properties	$k_{n,s,t}$	N/mm^3	10^6
Strength properties	$\tau^0_{n,s,t}$	MPa	73
Fracture energy	$G_{Ic,IIc,IIIc}$	J/m^2	300
Interaction parameter	η	–	2

(B–K) criterion [39] under mixed-mode loading shown in Eq. (9). Herein, G_I, G_{II}, and G_{III} signify the strain energy release rates under mode I, II, and III, while G_{Ic} and G_{IIc} denote critical strain energy release rates, and η embodies an interaction parameter.

$$G_c = G_{Ic} + (G_{IIc} - G_{Ic}) \left(\frac{G_{II} + G_{III}}{G_I + G_{II} + G_{III}} \right)^{\eta} \tag{9}$$

The interlaminar properties employed within this study are outlined in Table 2. The strength property $\tau^0_{n,s,t}$ and the critical strain energy release rates $G_{Ic,IIc,IIIc}$ values were taken from [40,41]. Furthermore, the interaction parameter η was obtained from [24,25]. In the absence of any known experimental studies characterising the employed composite material, specifically regarding the intralaminar properties essential for the VUMAT subroutine and the interlaminar properties required for modelling cohesive behaviour, and considering the variation found in literature regarding some of the material model constants, such as the fracture energies ($G_f^{1,2}$, $G_{Ic,IIc,IIIc}$), a preliminary parametric study was undertaken. This preliminary study aimed to refine the material properties to closely align with experimental evidence. Notably, in [25], the authors analysed the impact of interlaminar properties on the numerical predictions of impacted semi-cylindrical woven fabric composite shells involving E-glass/Polyester.

3.2. Geometric parameters and boundary conditions

The geometrical parameters of the specimens tested in [22] were considered during the formulation of the FE model. The specimens in question are characterised by a semicircular cross-sectional configuration, featuring an internal radius of 50 mm and a longitudinal length of 100 mm, as depicted in Fig. 3. Comprising the specimen's structure are 8 plain weaved composite fabric laminas, collectively yielding a composite thickness of 2.53 mm.

Two fixed rigid body supports, namely a lateral support and a bottom support, were added with the intention of emulating the supporting framework employed within the experimental context. In these experiments, the lower planar surfaces of the laminate, parallel with the xz-plane as illustrated in Fig. 3, were subjected to simple support conditions, while the vertical lateral supports, parallel with the yz-plane, were enacted to restrict displacements along the x-axis. By exploiting the geometric symmetries inherent in the model, a strategic reduction in computational expenses for the numerical investigations was achieved, resulting in the generation of solely one-quarter of the composite shell. Consequently, symmetry boundary conditions were imposed on the plane parallel to the yz-plane, as well as on one of the surfaces parallel to the xy-plane, as shown in Fig. 3.

The impactor is characterised by a lumped mass of 2.826 kg and featured a hemispherical head possessing a diameter of 10 mm. An impact velocity of 1.88 m/s was adopted, mirroring the impact energy of 5 J used in [22]. It is noteworthy that this energy level induces observable damage, without puncturing the specimens. Moreover, all the impactor's rotational degrees of freedom were constrained, and only the displacements along the y-axis were permitted. It must e emphasised that the velocity is predetermined and set as a field, diverging from the convention of defining velocity as a boundary condition with an amplitude derived from experimental characterisation. The significant advantage of this modelling approach lies in its independence from experimental velocity–time curves for each configuration, eliminating the need for such input in the FE model once validated for a particular configuration.
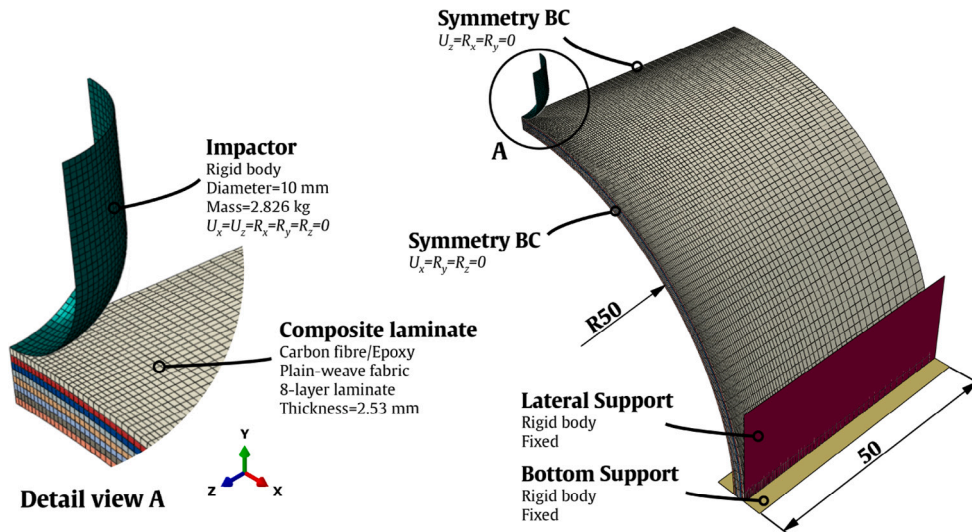
properties lacks standardised experimental procedures [29]. Furthermore, it is noteworthy that values documented in literature exhibit significant variability among different sources. Within the purview of this study, a good numerical–experimental correlation was discerned at $G_f^{1,2} = 2000$ J/m^2. It is important to highlight that this value was ascertained through a preliminary parametric study and falls within the spectrum of values delineated in [31,32] for woven-fabric reinforced composites.

To encompass the interlaminar damage, the adhesive interconnection among the laminas was modelled employing a surface-based cohesive damage model (S-BCM). The cohesive behaviour is governed by the traction τ-separation δ constitutive model illustrated in Fig. 2. The preliminary linear response, effective until the damage initiation is attained, is governed by the prescribed values of cohesive stiffness, k_n for normal and k_s, k_t for tangential directions. These parameters influence the performance of the FE model, with a variety of approaches available in the literature for their determination [33–36]. In the current study, the cohesive stiffness is set at 10^6 N/mm^3, in accordance with the recommendation of Camanho et al. [35]. Furthermore, it is assumed that this value remains uniform across all directions, i.e., $k_n = k_s = k_t$, as observed in a number of studies [24,25,36–38], yielding satisfactory results.

The ensuing stress-based quadratic failure criterion, expressed in Eq. (7), is employed to predict damage initiation. In this formulation, τ_n, τ_s, and τ_t correspond to the interface normal and shear contact stresses, while τ^0_n, τ^0_s, and τ^0_t denote the respective interface strengths. The Macaulay brackets $\langle \rangle$ indicate that the compressive stress does not contribute to damage. Upon the attainment of damage initiation, marked by the quadratic interaction function reaching a value of 1, the cohesive stiffness is degraded. Eq. (8) describes the softening response of the cohesive surface, with d denoting the damage coefficient.

$$\left(\frac{\langle \tau_n \rangle}{\tau^0_n} \right)^2 + \left(\frac{\tau_s}{\tau^0_s} \right)^2 + \left(\frac{\tau_t}{\tau^0_t} \right)^2 = 1 \tag{7}$$

$$\tau_i = (1 - d)\, k_i \delta_i \quad with \; i = n, s, t \tag{8}$$

The damage progression is controlled by the energy dissipated, quantified by G_c, representing the area under the $\tau - \delta$ curves depicted in Fig. 2. This fracture energy configuration defines the evolution of damage coefficients between the onset of damage and final failure. The computation of fracture energy G_c follows the Benzeggagh and Kenane

Fig. 3. Generated 3D FE model with indication of the dimensions, representation of the FE mesh discretisation, and imposed boundary conditions.

3.3. Mesh discretisation and element types

The woven fabric layers were modelled employing continuum shell elements (SC8R) featuring reduced integration and incorporating stiffness hourglass formulation. This choice of continuum shell elements is particularly apt for simulating impact scenarios, notably for its computational efficiency when contrasted with solid elements [42,43]. However, these elements have certain limitations, particularly in modelling complex geometries. Notably, they are not ideal for structures with a significant thickness-to-length ratio. Furthermore, continuum shell elements may not effectively capture both bending and stretching modes of deformation as comprehensively as solid elements [44]. In this context, the option for element deletion was deactivated, because the experimental observations from the impact tests on specimens did not register any puncturing [22].

The impactor was modelled employing discrete rigid elements (R3D4), while the supports were depicted as analytical rigid bodies. The modelling approach used for the supports, obviates the necessity for element and FE mesh specifications. Moreover, given the negligible interface thickness, it was modelled using cohesive surfaces, thus also avoiding the need for specific element definitions.

In order to find a balance between computational efficiency and the accuracy of numerical predictions, optimisation of the FE mesh discretisation is essential. This becomes particular significant for elements located in the vicinity of the impact region. The computation of fracture energy G_c in the interlaminar damage model, which results in delamination, is strongly influenced by the characteristic length of these elements [24,36]. Consequently, a seed was created along both the curved and straight edges of the semicylindrical shell to increase the FE mesh density at the impact region. Simultaneously, the density progressively decreases beyond this critical region. The FE mesh discretisation used in this study is represented in Fig. 3. It should be noted that a preliminary study was conducted by the authors to assess the FE mesh sensitivity in predicting the behaviour of semi-cylindrical composite laminate shells subjected to low-velocity impacts [24]. The study revealed that the FE mesh discretisation has a negligible impact on the maximum values obtained for the force, displacement, and contact time. However, it does affect the interlaminar damage initiation and progression. Therefore, in accordance with the considerations mentioned above, the FE mesh discretisation follows the recommendations presented in [24,36].

Consequently, the 8-layer FE model generated for this study incorporates 48 000 linear hexahedral elements type SC8R and 949 linear quadrilateral elements type R3D4. As previously noted, a seeding approach was employed, resulting in a non-uniform element size across the laminas. In the impact region, elements with an approximate global size of 0.3 mm were utilised, gradually increasing up to 2 mm in areas more distant from the impact region. Regardless of the stacking sequence under consideration, identical FE mesh discretisation, characterised by the same characteristic length and aspect ratio, was employed across all simulations. This approach ensures the comparability of predictions across different stacking sequences. To expedite solution computations, a semi-automated uniform mass scaling strategy was applied across the entire model. A target time increment of 10^{-7} s was adopted, culminating in a mass augmentation of 2.2%. Notice that the impact of mass scaling on simulations was analysed in [24]. This study revealed that the accuracy of dynamic response remains uncompromised for this percentage of mass augmentation, concurrently achieving up to 50% reduction in computational costs for solution calculations.

3.4. Contact definition

The penalty enforcement contact methodology, as implemented in ABAQUS/Explicit [26], was used to simulate the surface-to-surface interactions that arise between the semicylindrical composite shell, the metal impactor, and the metal supports [45]. Furthermore, this contact formulation was extended to the interface of the laminas, which, post-delamination, experience friction. The FE model was modelled such that all interfacing surfaces incorporate frictional interactions.

The friction coefficient values, denoted as μ, relevant to the metal-composite contacts and fully delaminated interfaces, were extracted from existing literature [24,25,46–48]. Subsequently, a value of $\mu = 0.3$ was stipulated for the contact between the hemispherical head of the impactor and the upper surface of the composite laminate. Moreover, the same value of $\mu = 0.3$ was employed for the interaction between the support surfaces and the composite laminate surfaces. Notice that the friction coefficient value assigned to the metal-laminate contacts was derived from [48]. The friction coefficient for the layers' interface was set at $\mu = 0.5$. While cohesive surfaces were assigned to all interface nodes initially in contact, a friction coefficient was incorporated to address the post-delamination friction that may occur within the delaminated areas. This is caused by the interfacial rubbing or sliding between the separated laminas as the material undergoes deformation. When the impact force induces delamination, the surfaces of the separated laminates can come into contact and experience relative motion. This relative motion generates frictional forces at the interface, leading
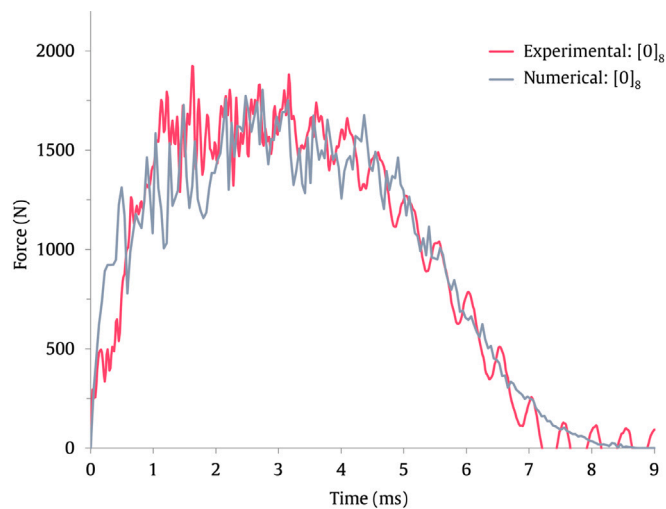
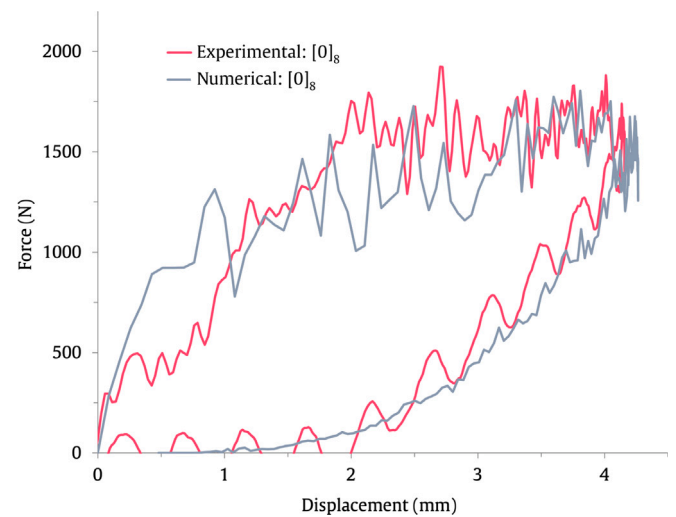**Fig. 4.** Numerical and experimental force-time results.

Fig. 5. Numerical and experimental force–displacement results.

to friction between the composite laminas. In this study, the specified coefficient value for interlaminar friction is consistent with the values proposed in [48,49].

4. Validation of the FE model

The objective of this section is to present the validation of the generated FE model of a $[0]_8$ laminate by juxtaposing the numerical predictions against the experimental evidence presented in [22]. Notice that only experimental data for the $[0]_8$ stacking sequence was available, restricting the scope for extending validation to other laminate configurations. Nonetheless, since the material properties were defined at the lamina level, with only their orientation changing in the various configurations, it is considered that this validation is adequate for the objectives of the present study. For this purpose, the numerical and experimental force-time, force–displacement and energy–time curves are depicted in Figs. 4–6, respectively. Additionally, Table 3 provides a succinct and informative snapshot of FE model's performance, comparing the predicted maximum force, maximum displacement and elastic energy (rebound energy) to the experimental data. It should be noted that the analysis of the coefficient of variation shows that the values obtained for the maximum force and displacement are less than 3%, revealing a low dispersion, while for the elastic energy is around 32%, leading to a large dispersion. In fact, the force and displacement behaviours were expected to be very close to each other because the selected impact velocity was low (and always the same) and the impactor diameter was relatively small. On the other hand, the large dispersion observed in terms of elastic energy is explained by the triggering of internal damage which is very sensitive to possible damage to the composite components, any defects introduced during the manufacturing process, and/or geometrical imperfections in the composite shell.

Overall, it is possible to appreciate a good numerical–experimental correlation for the force and energy history curves in Figs. 4–6. Moreover, it also possible to verify that they present the typical behaviour reported in literature for low-velocity impacts [50,51]. According to the literature [52], the maximum force value is a very important parameter as it depends on the impact energy and represents the peak load that the composite can withstand. Notably, the numerically predicted maximum force attains a satisfactory agreement with the experimental evidence, despite demonstrating a slightly lower value, characterised by a limited error margin of −7.9%. This discrepancy can, in part, be attributed to oscillations that arise from elastic wave and the consequential vibrations encountered in the composite specimens [53,54],

as discerned through the force-time curves presented in Fig. 4. The maximum displacement and the elastic energy values, presented in Table 3, yield a good agreement. The maximum displacement presents a negligible error of +1.7%, while the elastic energy, which corresponds to the difference between the absorbed energy and the energy at the maximum impact force [50], showcases an error of +6.9%.

It is important to underscore that the total energy, referred to in ABAQUS/Explicit [26] as output ETOTAL, exhibits steadfast stability, signifying the accurate definition of step time increments. Furthermore, the external energy, ALLAE output, is a minor fraction of the internal energy, ALLIE output. This observation underscores the appropriateness of the hourglass control method implemented.

While certain deviations are discernible, predominantly in the context of maximum force, the overall agreement underscores the FE model's efficacy in capturing the impact response of the tested semi-cylindrical composite shells. On the other hand, given the curved shell configuration of the specimens, experimentally observe the damage mechanisms, poses a significant challenge. Moreover, unlike fibreglass composites, the non-translucent nature of the carbon fibres hinders direct visual inspection, limiting the application of many non-destructive techniques for detailed micro-damage analysis. Fig. 7 shows the macro-level damage induced by the impact force, indicating its confined location within the impact region. According to the literature, the damage develops essentially along the thickness in the form of delaminations, with the maximum affected area occurring on the upper surface [18, 22]. Furthermore, it is well reported that increased thickness correlates with smaller damage areas due to the relationship between damage size and total dynamic deformation [18]. Notably, Fig. 7 reveals an apparent symmetry in the damage pattern, which is a consistent observation when comparing damage across various thicknesses in similar composites involving fibreglass, as studied in [16].

5. Parametric study

In this section the parametric study that was conducted to examine the effect of the stacking sequence on the dynamic response of semicylindrical composite shells under low-velocity impact loads is presented. For this purpose, a total of nine distinct stacking sequences were considered, as depicted in Fig. 8. Among these, the initial subset of five, labelled from A to E, were generated to study the effect of the layer orientations, encompassing angles of 0°/90°, ±45°, ±15°, ±22.5° and ±30°, respectively. The following contracted nomenclature was used to define each stacking sequence: $[0]_8$, $[45]_8$, $[+15,-15]_{2S}$, $[+22.5,-22.5]_{2S}$, and $[+30,-30]_{2S}$.

Table 3
Comparison between numerical predictions and experimental results [22] for the 8-layer composite shell (maximum force, maximum displacement, and elastic energy).

Maximum force			Maximum displacement			Elastic energy		
Numerical (N)	Experimental (N)	Error (%)	Numerical (mm)	Experimental (mm)	Error (%)	Numerical (J)	Experimental (J)	Error (%)
1804	1959 ± 50	−7.9	4.27	4.2 ± 0.02	+1.7	1.24	1.16 ± 0.38	+6.9
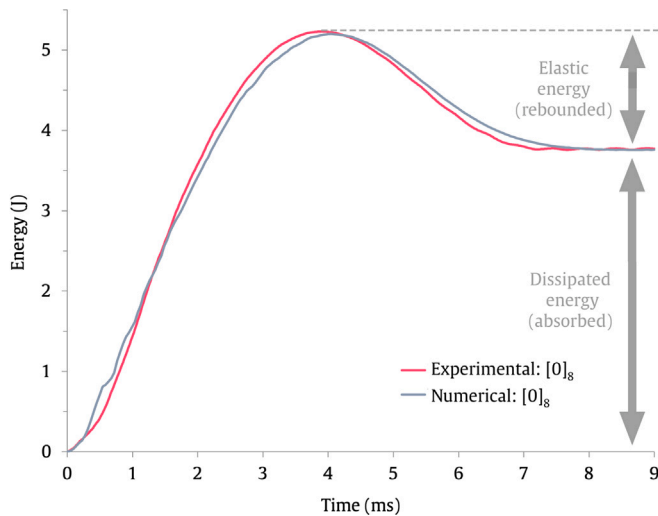
Fig. 6. Numerical and experimental energy–time results.

Detail view A
2:1
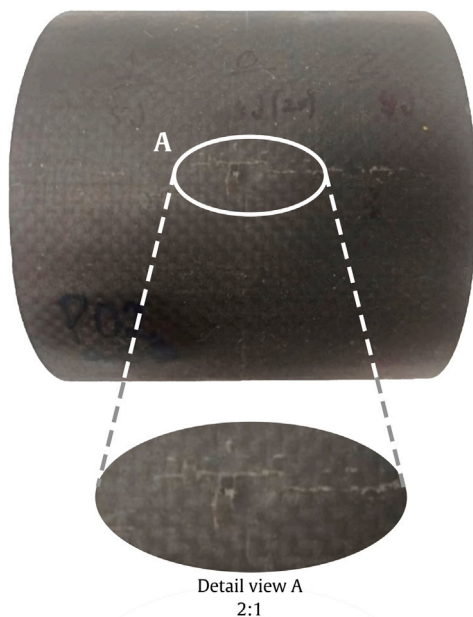
Fig. 7. Representation of the damage induced by an impact energy of 5 J in a semi-cylindrical composite shells specimen.

In the case of stacking sequences A and B, all the constituent layers are aligned with the same axis (referred to as single direction), whereas for C, D and E, the layers are aligned with two different axis (referred to as two directions), specifically ±15°, ±22.5° and ±30°. These latter stacking sequences yield angular amplitudes of 30°, 45° and 60°, as schematically represented in Fig. 9. It is worth noting that employing a simple approach, such as the analytical predictive tool CLT, which

based on Love–Kirchhoff model [55], any adjustment to the orientation angles of the fibres impacts the apparent in-plane stiffness properties of the layers/laminates. Specifically, the elastic moduli of the layers $E_{1,2}$ and of the laminates $E_{1,2}^L$ experience a reduction as the angle increases, accompanied by a corresponding increase in the shear modulus, $G_{1,2}$ and $G_{1,2}^L$, respectively. The changes in the elastic moduli and shear modulus, both for individual layers and for the laminates denoted as A, B, C, D, and E, are illustrated in Fig. 10. Consequently, it is anticipated that these changes in the in-plane stiffness properties of the layers/laminates affect the dynamic response of the composite shell under impact loading conditions.

Concurrently, the subsequent four stacking sequences, labelled F, G, H and I, with the contracted nomenclature, $[0_2,45_2]_S$, $[0,45]_{2S}$, $[0,45_2,0]_S$, and $[45_2,0_2]_S$, respectively, were chosen to analyse the impact response in semicylindrical quasi-isotropic laminate shells, and the consequential effects of interchanging the layer's positioning about the mid-plane. Moreover, this analysis intends to ascertain any potential associations of the number of angle mismatching interfaces with the interlaminar damage (delaminations).

6. Results and discussion

In this section, the numerically predicted results regarding the impact response of the stacking sequences detailed in Section 4, with specific focus on the effect of the layers orientation (stacking sequences A, B, C, D and E) and positioning within the laminate (stacking sequences F, G, H and I), are presented and discussed.

6.1. Effect of the layer's orientation

The effect of the layer's orientation in the impact response of semi-cylindrical composite laminate shells is analysed employing stacking sequences in which all woven fabric layers are either aligned along a single axis (subset comprising A and B) or distributed across two distinct axes (subset comprising C, D, and E).

The numerically predicted force-time and force–displacement curves pertaining to stacking sequences A and B are depicted in Figs. 11 and 12. Similarly, for stacking sequences C, D, and E, representations of these curves are presented in Figs. 13 and 14. In order to facilitate a direct and comprehensive comparison with the validated FE model, the results of stacking sequence A were included in most of the figures that characterise the impact response of the composite shell. The discernible oscillations evident in the curves can be attributed to the vibrations of the composite shells during the impact event, as substantiated in [53,54]. Noticeably, all the obtained curves present the characteristic response pattern associated with low-velocity impacts, wherein no puncturing occurs [24,50,52]. Irrespective of the specific stacking sequence, a discernible behaviour emerges in all force-time curves, marked by an increase in force culminating in the attainment of a maximum value denoted as F_{max}, followed by a subsequent decline. In accordance with the existing literature [52], F_{max} serves as an indicator denoting the maximum force the composite shell can endure when subjected to a specified impact energy threshold, prior to incurring significant damage.

In this context, Table 4 provides the maximum force values for the various stacking sequences studied. Moreover, the values obtained for
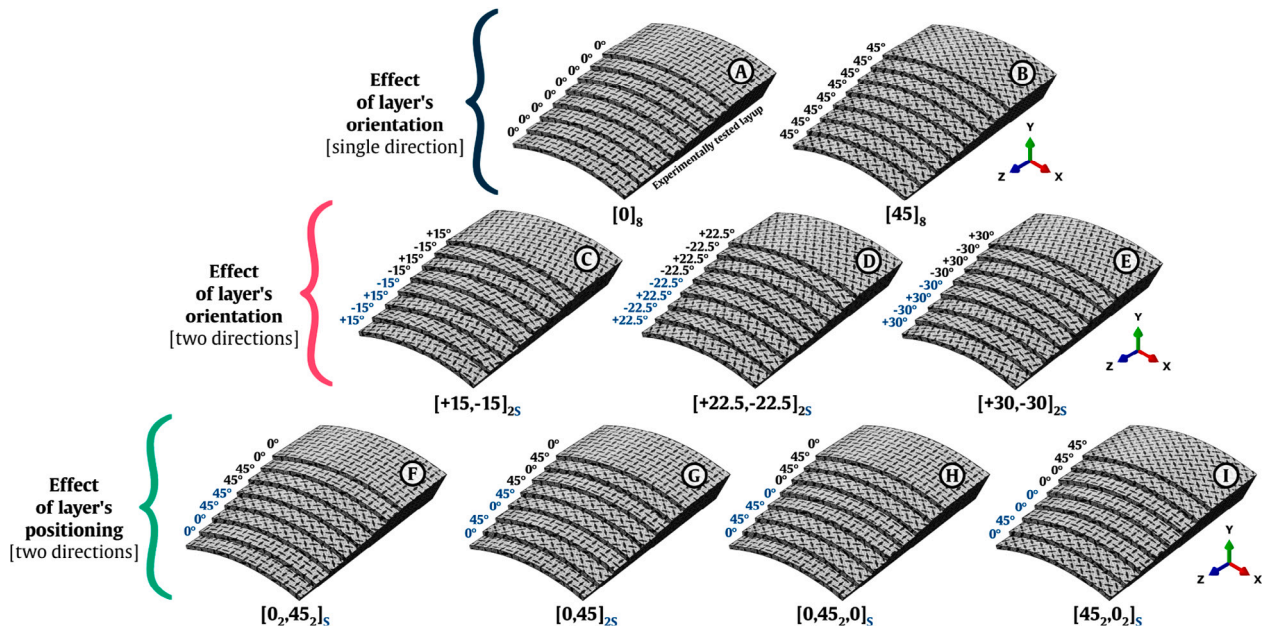
Fig. 8. Stacking sequences considered to numerically study the effect of the layers orientation and positioning in the impact response of the semicylindrical composite shell.
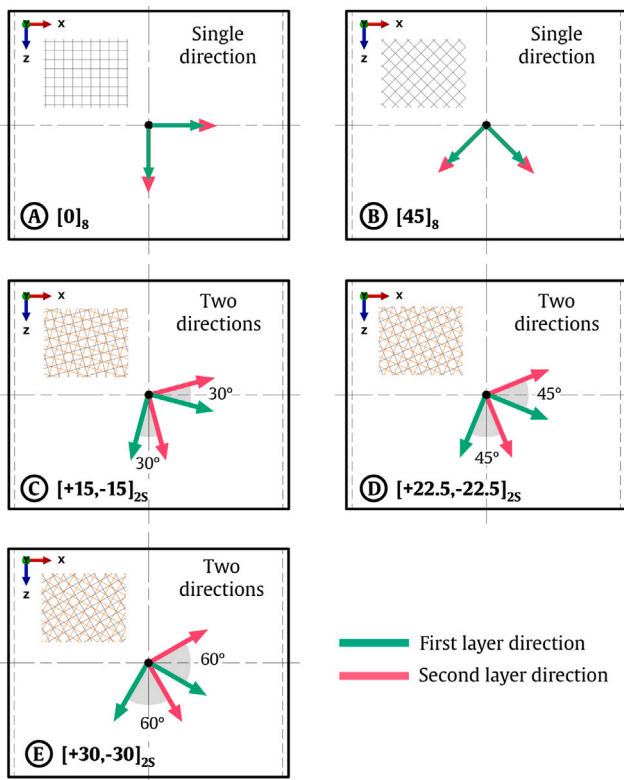

Fig. 9. Top view of the FE model with the first and second layer orientations for the configurations A to E, and the corresponding amplitude of the angle relative to the axis of the semicylindrical shell.

Fig. 10. Apparent in-plane stiffness properties of a single layer ($E_{1,2}$, $G_{1,2}$) and of the laminates ($E_{1,2}^L$, $G_{1,2}^L$), for the considered angle orientations/stacking sequences, calculated according to the CLT.

the maximum displacement, contact time, dissipated energy, and the IBS, are also presented. Notice that the dissipated energy (absorbed energy) is derived from the energy–time curve extracted from the ABAQUS output ALLKE - Kinetic energy. The corresponding value is obtained as shown in Fig. 6. Additionally, the IBS was derived from the initial slope of the force–displacement curves represented in Figs. 12,

14 and 20, and its value can be used to evaluate the damage resistance of composite laminates [16,56]. The data presented in Table 4 underscores that having the woven fabric layers aligned with a single axis or in two different axis exerts a discernible influence on all the analysed impact parameters. Stacking sequences characterised by the alignment of all woven fabric layers along a single axis (A and B), manifest lower F_{max} values when contrasted with those with layers aligned along two distinct axes (C, D, and E). Conversely, the former configurations exhibit higher values in terms of maximum displacement and contact time. These differences between the two subsets of stacking sequences are associated with the distinct stiffnesses exhibit by the laminates, as quantified by their respective values of IBS. The increase of the IBS is accompanied by an increase of the maximum force and decrease of the maximum displacement and contact time. Notice that a similar trend was observed by Kistler in [57] for cylindrical composite shells. Moreover, the results are in the agreement with the observations made by Wu et al. in [58]. Their study compared braided composite plates
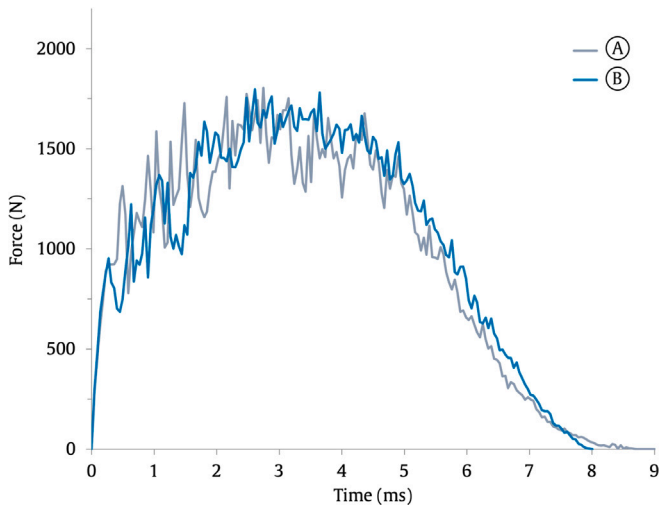
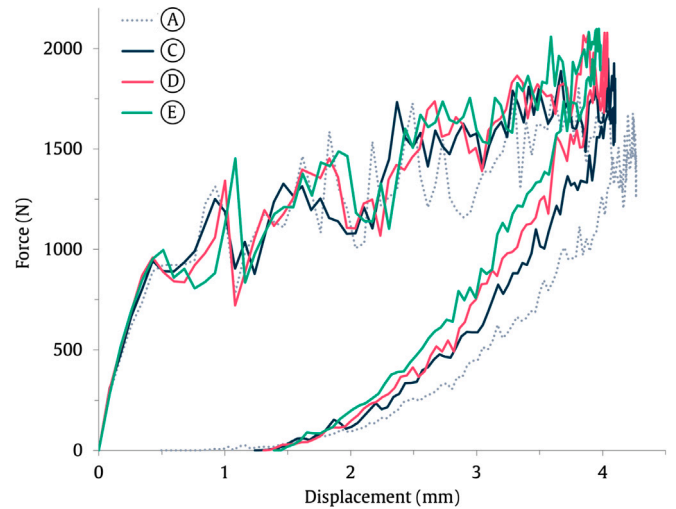**Fig. 11.** Force-time results for stacking sequences A and B.

Fig. 12. Force–displacement results for stacking sequences A and B.
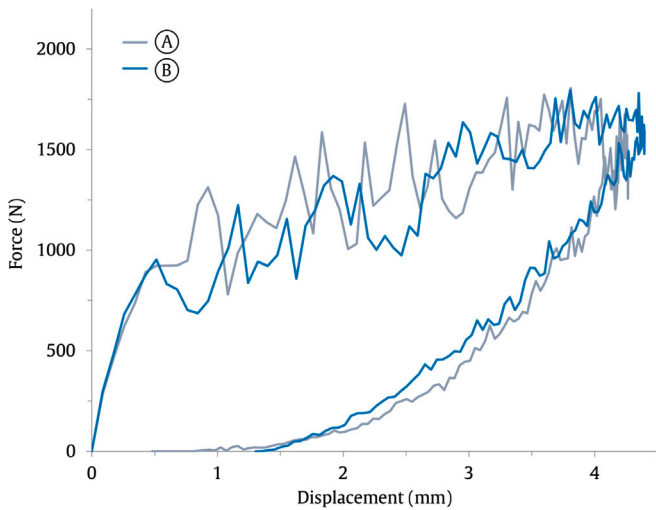

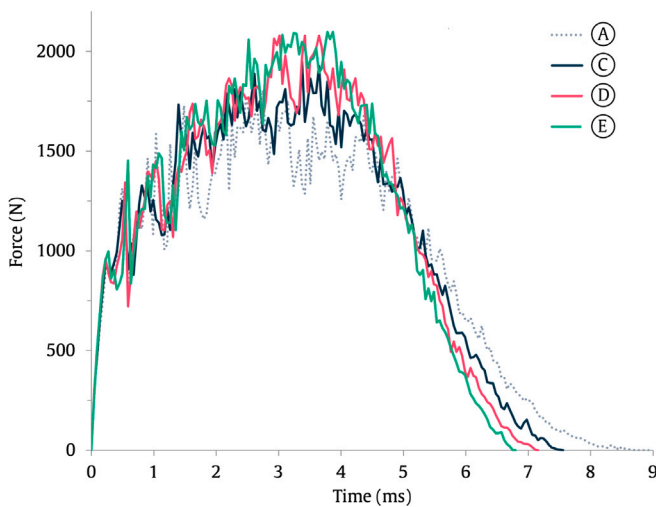**Fig. 13.** Force-time results for stacking sequences C, D and E.

Fig. 14. Force–displacement results for stacking sequences C, D and E.

with fibre orientation angles of 0°, 22.5°, and 45°, and their results indicated that the specimens with fibres oriented at 22.5° orientation displayed the highest maximum impact force and lowest maximum displacement.

Upon comparing the subset comprising of stacking sequences C, D and E, it is possible to appreciate that increasing the amplitude angle corresponds to concurrent increase in the IBS. The difference reaches about 6.7% between stacking sequences C and E. Again, it is apparent that the increase in stiffness yields a corresponding increase in the maximum force, accompanied by a reduction in both the maximum displacement and contact time. The differences reach up to approximately 7.3%, 10.6% and 7.9% for the maximum force, maximum displacement and contact time, respectively.

Noticeably, the IBS of stacking sequence A is approximately 4.5% higher than that of stacking sequence B. This leads to a marginal increase in the maximum force, about 0.4%, while simultaneously inducing a reduction in the maximum displacement, approximately −2.7%. It is noteworthy that while this behaviour aligns with the previous findings concerning these parameters in relation to changes in IBS, the contact time exhibits a distinct pattern by increasing approximately 7.8%.

Collectively, the results underscore the significant enhancement in the laminate's resilience to impact loads when utilising layers with woven fabrics aligned along two distinct axes, in contrast to configurations aligning them along a single axis. Furthermore, an evident correlation emerges: as the amplitude of the axis angle increases, the IBS experiences also an increase. Notably, the disparities observed between these two subsets are relevant, with maximum differences reaching approximately 15.5%, 9.8%, and 24.9% for the maximum force, maximum displacement, and contact time, respectively.

During a low-velocity impact event without puncture, impact energy undergoes complete transfer to the laminate. This energy is partially stored as elastic energy and partially dissipated as intralaminar damage (comprising fibre and matrix failure), interlaminar damage (delaminations), and friction generated during interactions between involved components. Since puncturing does not occur, most of the elastic energy is subsequently recovered and redirected to the impactor as it rebounds from the composite laminate shell. A small portion of energy is transformed into vibrations, which are then damped over an extended timescale. Fig. 15 shows the numerically predicted energy history curves for stacking sequences A to E, and Table 4 provides the values of the dissipated (absorbed) energy for each stacking sequence.

The energy–time curves distinctly reveal that stacking sequence A dissipates a greater amount of energy compared to all the other stacking

Table 4

Numerical predictions of the maximum force, maximum displacement, contact time, dissipated energy, and IBS, and number of angle-mismatch interfaces for the different stacking sequences considered.

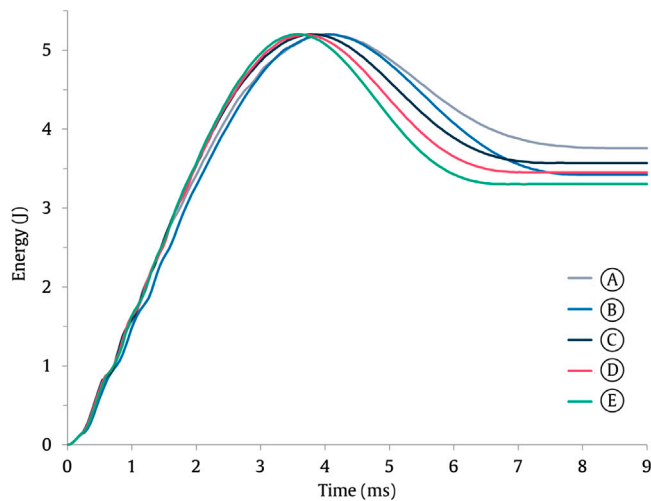| Stacking sequence	Mismatch interfaces	Maximum force (N)	Maximum displacement (mm)	Contact time (ms)	Dissipated energy (J)	IBS (N/mm)
A	0	1804	4.27	8.73	3.76	489
B	0	1796	4.39	8.10	3.42	468
C	6	1950	4.10	7.56	3.57	522
D	6	2078	4.04	7.16	3.45	547
E	6	2097	3.98	6.80	3.30	558
F	2	2008	3.97	7.52	3.63	548
G	6	2038	4.04	7.83	3.65	540
H	4	1941	4.04	7.79	3.60	522
I	2	1863	4.22	8.15	3.44	498

Fig. 15. Energy–time results for stacking sequences A, B, C, D and E.
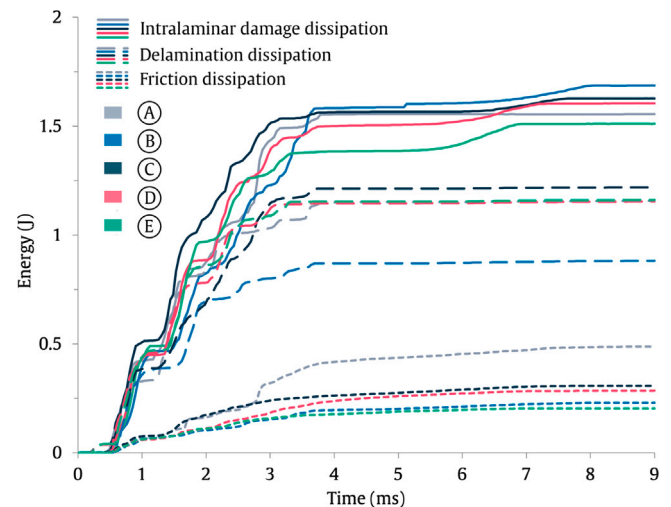

Fig. 16. Energy–time results for stacking sequences A, B, C, D and E.

sequences. A pronounced disparity emerges when contrasting the two stacking sequences with woven fabric layers aligned in a single axis, namely A and B, with a noticeable difference of approximately 9.5%. In the case of stacking sequences C, D, and E, it becomes evident that an increase in the amplitude angle corresponds to a reduction in the dissipated energy. For instance, the energy dissipation exhibited by E is approximately −7.6% lower than that of C. This behaviour was also observed in braided composite plates in [58].

To better understand the mechanisms associated with the energy dissipation, Fig. 16 plots the evolution of the dissipated energy throughout the impact time, due to intralaminar damage, delaminations, and friction. The various mechanisms of energy dissipation were extracted from the following different ABAQUS outputs: intralaminar damage (ALLPD – Plastic dissipation), interlaminar damage (ALLDMD – Damage dissipation) and friction (ALLFD - Frictional dissipation). Notably, the intralaminar damage takes precedence as the primary damage mode, followed by delaminations. Intralaminar damage accounts for about 29% to 32.5% of the total impact energy, while delaminations range from about 16.9% to 23.5%. Stacking sequence B demonstrates the highest intralaminar damage dissipation and the lowest delamination dissipation. Conversely, E exhibits the lowest intralaminar damage dissipation, while C has the highest delamination dissipation. The observations regarding intralaminar damage are in concurrence with the findings of Zhang et al. as reported in their study [59]. In their investigation into the impact response of woven composite plates and its relationship with off-axis angles, they noted that the specimens with a 45° orientation exhibited a greater degree of intralaminar damage compared to those oriented at 0°.

While the energy dissipation results from stacking sequences A and B do not reveal a discernible trend linked to the IBS, the observations stemming from stacking sequences C, D, and E show that the increase

in stiffness corresponds to a decrease in the energy dissipated by intralaminar damage, alongside an increase in the energy dissipated through delaminations. These findings align with the research conducted by Amaro et al. [60], wherein it was ascertained that the low deflection exhibited by composite shells, a characteristic associated with heightened structural stiffness, can justify the substantial energy dissipation attributed to delaminations. It should also be noted that for these stacking sequences, the number of angle-mismatched interfaces has no discernible influence on energy dissipated by delaminations.

Additionally, it can be appreciated that the energy dissipated through friction cannot be neglected. For stacking sequences A and B, it constitutes approximately 9.4% and 4.4% of the total impact energy, respectively. For C, D and E, it is observed that the increase in IBS results in a reduction of the energy dissipated through friction, with values ranging from 5.9% to 3.9%.

In Fig. 17, a detailed depiction of the percentage of energy dissipated by each layer due to intralaminar damage, for stacking sequences A to E, is presented. The allocation of dissipated energy remains consistent across all stacking sequences, with the two upper layers exhibiting the highest levels of energy dissipation (highlighted in red), while the two lower layers contribute the least to this dissipation (highlighted in green). For all stacking sequences, the upper half of the laminate (layers #1 to #4) is responsible for about 60% of all the dissipated energy by intralaminar damage, albeit with an exception noted for B, which dissipates slightly less, approximately 57%.

The observations pertaining to the failure modes can also be discerned in Fig. 18, where the intralaminar damage (encompassing tensile/compressive damage along the fibre directions and shear damage) and delaminations are plotted across the FE models featuring stacking sequences A to E. It can be appreciated that the generated FE models
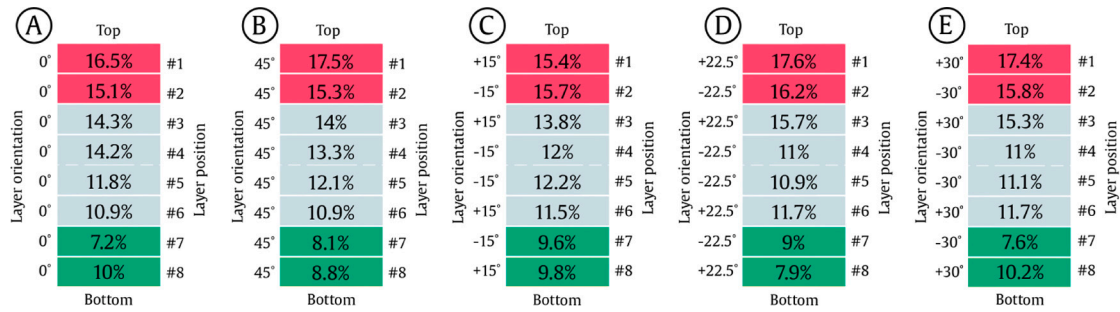
Fig. 17. Energy dissipated by each layer due to intralaminar damage, for stacking sequences A, B, C, D and E.

are capable of predicting the different damage modes for the distinct layer orientations considered. The stacking sequences exhibit different impact footprints, and the damage extent of the two failure models agrees with the findings described for Fig. 16. Moreover, the results show that damage is restricted to the impact location in the form of fibre failure and delaminations, as found in the experimental evidence for the 8-layer laminates [22]. These results, in conjunction with the observations delineated in Fig. 17, align closely with the research findings reported by Giancaspro et al. [61]. Their study corroborated that in composites subjected to bending modes, carbon fibres predominantly undergo failure on the compression side (upper layers). Furthermore, although the damage introduced differs in typology and size for the different stacking sequences, as shown in Fig. 18, the force-time and force–displacement curves do not reveal very significant differences between them. This can be explained by the fact that the impact velocity is constant and small in magnitude (much lower than the perforation value), in addition to the impactor having a small diameter. In this context, as shown in Fig. 7, the damage is confined to the impact region and propagates essentially along the thickness, which can be corroborated by Fig. 18. On the other hand, the differences in the damage observed result from the different stacking sequences which, according to the literature [8,9,11,12], have a decisive influence on the type and size of the damage. This is because they have different impact bending stiffness values between each group of equally oriented layers, coupled with the fact that the grouping of layers promotes an increase in bending stiffness and stress concentration at the interfaces [8,13].

6.2. Effect of the layer's positioning

The analysis in this section pertains to the interchanging of the position of layers about the mid-plane of the quasi-isotropic stacking sequences denoted from F to I, as depicted in Fig. 8. Consequently, simulations were conducted to predict the impact response of these semicylindrical composite shells and to ascertain any potential associations with the arrangement of the layers and/or the number of angle mismatching interfaces.

To facilitate comparative assessment, Figs. 19, 20, and 21 present the low-velocity impact curves, encompassing force-time, force–displacement, and energy–time for stacking sequences F, G, H and I.

The force and energy history curves clearly demonstrate that stacking sequences F, G, and H exhibit similar impact responses. Furthermore, the results provided in Table 4 reveal that G generally yields higher values across most parameters when compared to F and H. Notably, the most significant difference for this subset occurs for the maximum force, between G and H, reaching about 4.9%. The remaining parameters, including maximum displacement, contact time, dissipated energy, and IBS, exhibit negligible variations, with differences not exceeding 1.7%. In contrast, stacking sequence I displays a discernibly impact response. It registers the lowest IBS which results in lower maximum force and higher maximum displacement and contact time values. This behaviour agrees with the findings discussed in Section 6.1 for stacking sequences C, D and E, and with literature [57]. The most
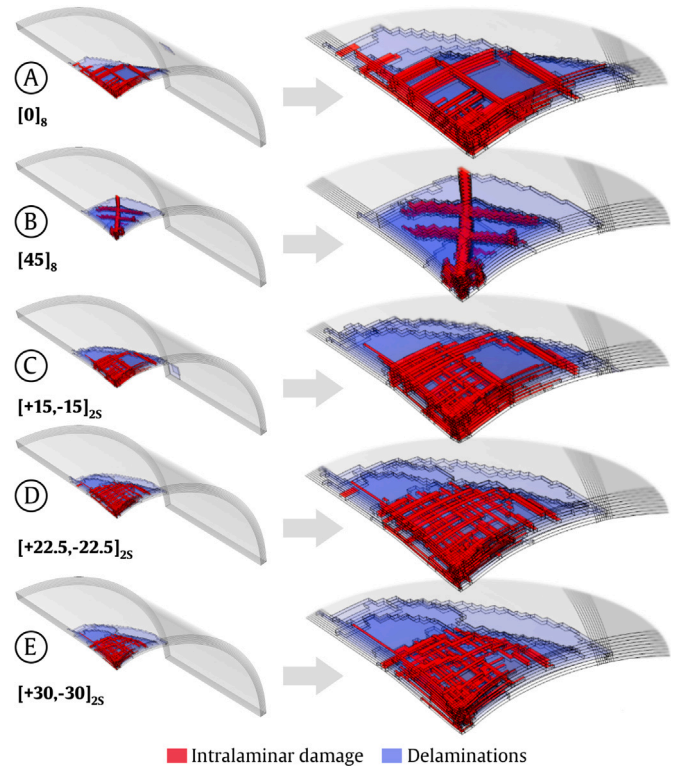

Fig. 18. Intralaminar damage and delaminations throughout the semicylindrical composite shells (configurations A to E), with the corresponding detail views of the damage footprint.

substantial disparities in the impact results, as presented in Table 4, emerge mostly between F and I, except for the maximum force, where the most significant difference is observed between G and I. Notably, the most pronounced disparities were observed in the case of the IBS, maximum force, and contact time, registering substantial differences of 9.6%, 9%, and 8%, respectively. Regarding the energy dissipation, stacking sequence I dissipates about −5.8% than G.

It is essential to acknowledge that these findings do not align with what was reported by Singh and Mahesh in [7], which explored the impact of interchanging the positions of woven glass fibre (0°/90°) and (±45°) layers in flat plates. Their research indicated that stacking sequence $[0,45_2]_S$, corresponding to configuration H, exhibited the highest maximum force and minimum displacement. Furthermore, within the same study, Singh and Mahesh [7] advocated the utilisation of the determinant of the bending stiffness matrix to ascertain the optimal stacking sequence for the quasi-isotropic composites when subjected to low-velocity impacts. However, it is noteworthy that the present study did not reveal any discernible correlation between the bending stiffness matrix of the composite laminate and the analysed
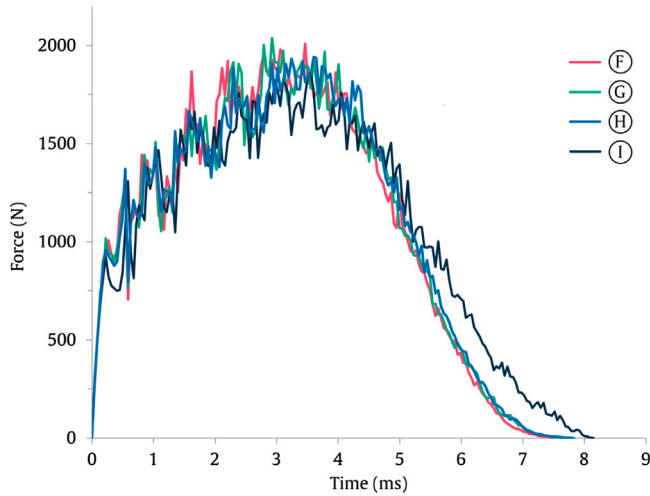
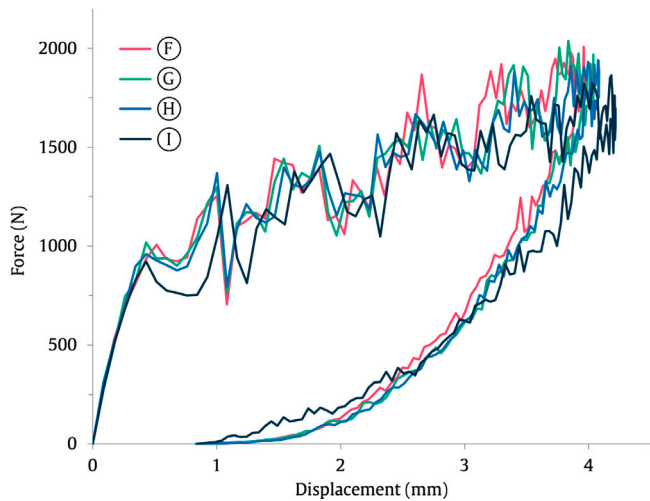**Fig. 19.** Force-time results for stacking sequences F, G, H and I.

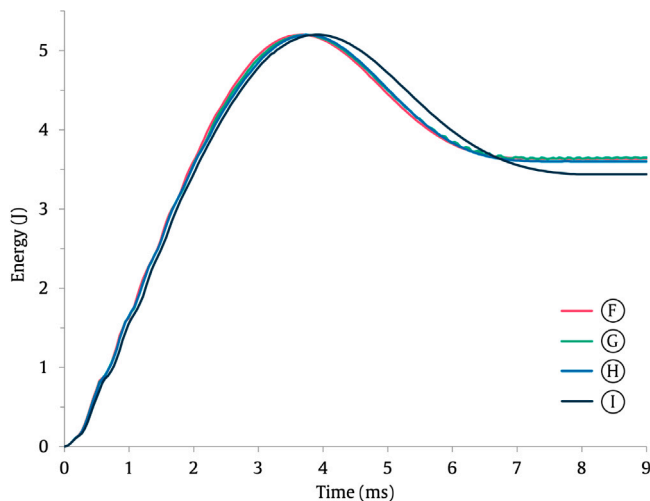**Fig. 20.** Force–displacement results for stacking sequences F, G, H and I.

Fig. 21. Energy–time results for stacking sequences F, G, H and I.
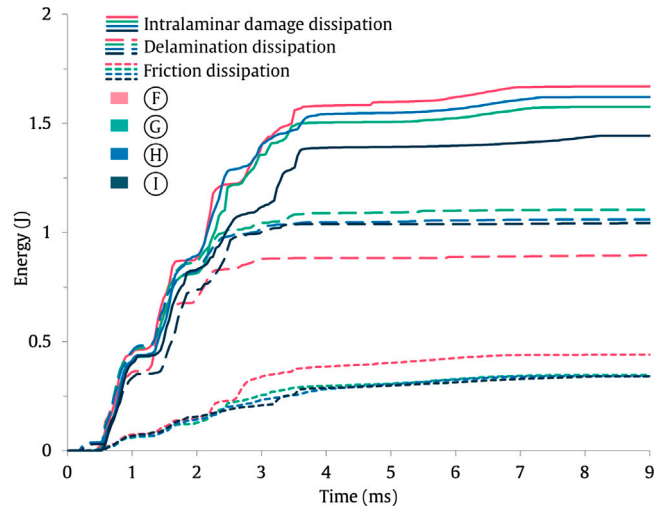

Fig. 22. Energy–time results for stacking sequences C, D and E.

impact parameters. For example, despite the fact that the calculated determinant of the bending stiffness matrix for stacking sequences F and I being identical, the numerically predicted results exhibit considerable disparity, as detailed earlier.

Fig. 22 provides insights into the energy balance for these stacking sequences. The results underscore, once again, that the majority the impact energy is dissipated by intralaminar damage, followed by delaminations and friction. Intralaminar damage accounts for 27.8–32.1% of the total impact energy, while delaminations account for 17.2–21.2%. The energy dissipated thought friction is also influenced by the positioning of the layers and cannot be neglected. For stacking sequence F, it represents 8.5% of the total impact energy, and for the remaining stacking sequences it represents about 6.6%.

Stacking sequence F exhibits the highest amount of energy dissipated by intralaminar damage, and the lowest by delaminations. On the other hand, stacking sequence I has the lowest intralaminar damage dissipation, and G the highest delamination dissipation. Conversely to what was observed for C, D and E, the increase in the IBS leads to an increase in the energy dissipated by intralaminar damage, alongside an decrease in the energy dissipated through delaminations. In the context of delaminations, the discrepancy in the number of angle-mismatched layers may underlie the variations found for the different stacking sequences. For example, stacking sequence G, features six angle-mismatching interfaces and records the highest energy dissipated by delamination, while F, with only two angle-mismatching interfaces, registers the lowest.

Fig. 23, illustrates the percentage of energy dissipated by individual layers attributed to intralaminar damage, from stacking sequences F, G, H and I. Within each stacking sequence, the two layers that exhibit the highest and lowest percentages of energy dissipation are highlighted in red and green, respectively. It becomes evident that altering the positioning of the layers in the semicylindrical quasi-isotropic composite shell exerts a substantial influence on the distribution of energy dissipated by each layer. Across all these stacking sequences, the 45°-oriented layers emerge as the primary contributors to energy dissipation, particularly when situated in the upper half of the laminate, spanning layers #1 to #4. Conversely, the 0°-oriented layers in the lower half of the laminate, spanning layers #4 to #8, exhibit the lowest levels of energy dissipation attributable to intralaminar damage. The upper half of stacking sequences F, G, H and I dissipate about 58%, 59%, 63% and 69% of the energy, respectively. The increase observed for stacking sequence I can be justified by the presence of two 45° layers on positions #1 and #2 of the laminate. Furthermore, it is evident that stacking sequence F has a more equitable distribution of

Fig. 23. Energy dissipated by each layer due to intralaminar damage for stacking sequences F, G, H, and I.
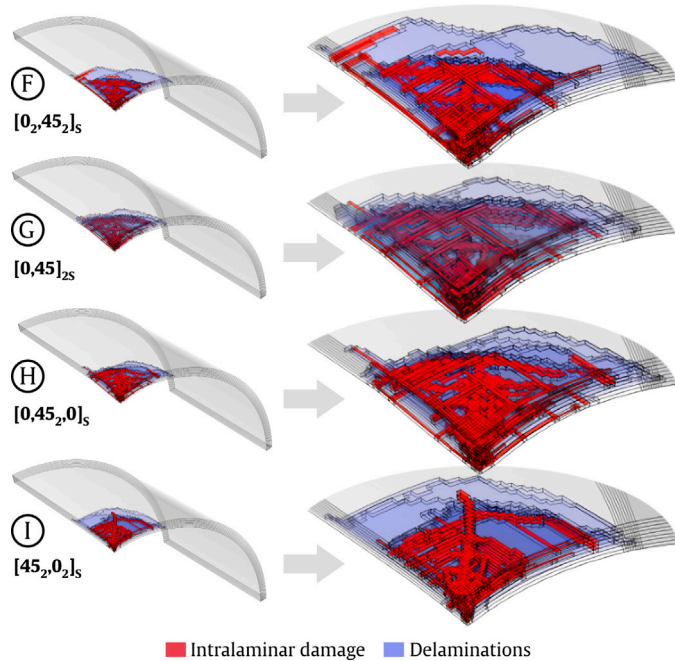

Fig. 24. Intralaminar damage and delaminations throughout the semicylindrical composite shells (F to I), with the corresponding detail views of the damage footprint.

the percentage of intralaminar damage dissipation among its layers, thereby promoting a more balanced response. In contrast, stacking sequence I exhibits the most unbalanced distribution. This divergence in balance is corroborated by the standard deviation of the percentage of energy dissipated, standing at approximately 3% for stacking sequence F and notably higher at 6.1% for stacking sequence I. Meanwhile, stacking sequences G and H display analogous deviations, both around the 5%.

The numerically predicted failure modes across the different layers of the laminates, are depicted in Fig. 24. It can be appreciated once again that the generated FE models are capable of predicting the different damage modes for the distinct layer orientations considered. The stacking sequences exhibit different impact footprints, and the damage extent of the fibre failure and delaminations agrees with the findings described for Fig. 22. Moreover, the results show that damage is restricted to the impact location.

These findings underscore the impact of interchanging the layer positioning on the overall response of the quasi-isotropic composite shells to low-velocity impact loads.

7. Conclusions

This study was conducted to investigate the effect of the stacking sequence on the impact response of semicylindrical woven composite shells. Specifically, the influence of layers orientations and its positioning with respect to the laminate's mid-plane were analysed. In the first case, the layers were aligned with the axes of the two directions (X and Y) promoting stacking sequences that led to angular amplitudes of 30°, 45° and 60°, while the second case aimed to investigate possible associations between the number of angles mismatching interfaces and the interlaminar damage.

Regarding the layers orientation, the findings revealed that stacking sequences with all woven fabric layers aligned along a single axis ($[0]_8$ and $[45]_8$) resulted in lower maximum force values but higher maximum displacement and contact time. This can be attributed to differences in stiffness. In terms of energy dissipation, $[0]_8$ laminates exhibited the highest dissipated energy, whereas laminates aligned along two different axes showed reduced dissipated energy as the amplitude angle increased. Our analysis also revealed that intralaminar damage accounted for approximately 29% to 32.5% of the total impact energy, delaminations for approximately 16.9% to 23.5%, and friction for approximately 3.9% to 9.4%, depending on layer orientation.

Regarding the study related to layer positioning, sequences such as $[0_2,45_2]_S$, $[0,45]_{2S}$, $[0,45_2,0]_S$, and $[45_2,0_2]_S$ exhibited similar impact responses in terms of maximum force, displacement, contact time, and dissipated energy. The most significant difference was observed in the maximum force (approximately 4.9%), with other parameters showing negligible variations (less than 1.7%). However, it is important to note that altering layer positioning significantly influenced the energy dissipation by each layer. Regarding the intralaminar damage, it contributed approximately 27.8% to 32.1% of the total impact energy, delaminations approximately 17.2% to 21.2%, and friction approximately 6.6% to 8.5%. Although these differences were observed for the different impact parameters, they took into account the fact that the impact velocity was always constant and of low magnitude. However, in the future, it is suggested to study its influence on the various impact parameters, especially at the level of damage to establish a relationship that allows the severity of the damage to be assessed depending on the impact velocity.

Finally, from a global perspective, this study provides a numerical tool to assist designers in assessing the effect of stacking sequence on impact response of semicylindrical woven composite shells. The validation of the FE models employed presents an opportunity to reduce dependence on costly and time-consuming experimental testing. The FE models were able to capture the damage mechanisms and provide detailed information about impact response for this type of composite structures. Such information can be leveraged to enhance design guidelines, formulate effective mitigation strategies, and optimise the performance and reliability of laminated shell structures.

CRediT authorship contribution statement

L.M. Ferreira: Writing – review & editing, Writing – original draft, Validation, Software, Methodology, Investigation, Formal analysis, Data curation, Conceptualization. **M. Muñoz-Reja:** Writing – review & editing, Validation, Formal analysis. **P.N.B. Reis:** Writing – review & editing, Writing – original draft, Validation, Supervision, Investigation, Formal analysis, Conceptualization.

Declaration of competing interest

The authors declare that they have no known competing financial interests or personal relationships that could have appeared to influence the work reported in this paper.

Data availability

Data will be made available on request.

Acknowledgments

References

[1] Adams R, Cawley P. A review of defect types and nondestructive testing techniques for composites and bonded joints. NDT Int 1988;21(4):208–22. http://dx.doi.org/10.1016/0308-9126(88)90333-1.

[2] Papa I, Ricciardi M, Antonucci V, Langella A, Tirillò J, Sarasini F, Pagliarulo V, Ferraro P, Lopresto V. Comparison between different non-destructive techniques methods to detect and characterize impact damage on composite laminates. J Compos Mater 2020;54(5):617–31. http://dx.doi.org/10.1177/0021998319864411.

[3] Duchene P, Chaki S, Ayadi A, Krawczak P. A review of non-destructive techniques used for mechanical damage assessment in polymer composites. J Mater Sci 2018;53(11):7915–38. http://dx.doi.org/10.1007/s10853-018-2045-6.

[4] Hodges J, Yates B, Darby MI, Wostenholm GH, Clemmet JF, Keates TF. Residual stresses and the optimum cure cycle for an epoxy resin. J Mater Sci 1989;24(6):1984–90. http://dx.doi.org/10.1007/BF02385410.

[5] Cho M, Kim M-H, Choi HS, Chung CH, Ahn K-J, Eom YS. A study on the room-temperature curvature shapes of unsymmetric laminates including slippage effects. J Compos Mater 1998;32(5):460–82. http://dx.doi.org/10.1177/002199839803200503.

[6] Svanberg J, Holmberg J. An experimental investigation on mechanisms for manufacturing induced shape distortions in homogeneous and balanced laminates. Composites A 2001;32(6):827–38. http://dx.doi.org/10.1016/S1359-835X(00)00173-1.

[7] Singh K, Mahesh. Effect of ply position switching in quasi-isotropic glass fibre reinforced polymer composite subjected to low velocity impact. Int J Damage Mech 2022;31(5):665–93. http://dx.doi.org/10.1177/10567895211068176.

[8] Riccio A, Di Felice G, Saputo S, Scaramuzzino F. Stacking sequence effects on damage onset in composite laminate subjected to low velocity impact. Procedia Eng 2014;88:222–9. http://dx.doi.org/10.1016/j.proeng.2014.11.148, International Symposium on Dynamic Response and Failure of Composite Materials, DRaF2014.

[9] Lin S, Waas AM. The effect of stacking sequence on the LVI damage of laminated composites; experiments and analysis. Composites A 2021;145:106377. http://dx.doi.org/10.1016/j.compositesa.2021.106377.

[10] Wu Z, Wu C, Liu Y, Cheng X, Hu X. Experimental study on the low-velocity impact response of braided composite panel: Effect of stacking sequence. Compos Struct 2020;252:112691. http://dx.doi.org/10.1016/j.compstruct.2020.112691.

[11] AhmadFurqan, HongJung-Wuk, Soap C, ParkSoo-Jin, Kyun P. The effects of stacking sequence on the penetration-resistant behaviors of T800 carbon fiber composite plates under low-velocity impact loading. Carbon Lett 16(2):107–15. http://dx.doi.org/10.5714/CL.2015.16.2.107.

[12] Lebaupin Y, Hoang T-QT, Chauvin M, Touchard F. Influence of the stacking sequence on the low-energy impact resistance of flax/PA11 composite. J Compos Mater 2019;53(22):3187–98. http://dx.doi.org/10.1177/0021998319837339.

[13] Fuoss E, Straznicky PV, Poon C. Effects of stacking sequence on the impact resistance in composite laminates — Part 1: parametric study. Compos Struct 1998;41(1):67–77. http://dx.doi.org/10.1016/S0263-8223(98)00036-1.

[14] Wu Z, Zhang Q, Li B, Liu Y, Pan Z. Transverse impact response and residual flexure characteristics of braided composite tubes: Effect of stacking sequence. Thin-Walled Struct 2020;155:106900. http://dx.doi.org/10.1016/j.tws.2020.106900.

[15] Ferreira L, Coelho C, Reis P. Numerical predictions of intralaminar and interlaminar damage in thin composite shells subjected to impact loads. Thin-Walled Struct 2023;192:111148. http://dx.doi.org/10.1016/j.tws.2023.111148.

[16] Reis P, Sousa P, Ferreira L, Coelho C. Multi-impact response of semicylindrical composite laminated shells with different thicknesses. Compos Struct 2023;310:116771. http://dx.doi.org/10.1016/j.compstruct.2023.116771.

[17] Reis PNB, Coelho CACP, Navalho FVP. Impact response of composite sandwich cylindrical shells. Appl Sci 2021;11(22). http://dx.doi.org/10.3390/app112210958.

[18] Zhao G, Cho C. Damage initiation and propagation in composite shells subjected to impact. Compos Struct 2007;78(1):91–100. http://dx.doi.org/10.1016/j.compstruct.2005.08.013.

[19] Ferreira L, Aranda M, Muñoz-Reja M, Coelho C, Távara L. Ageing effect on the low-velocity impact response of 3D printed continuous fibre reinforced composites. Composites B 2023;267:111031. http://dx.doi.org/10.1016/j.compositesb.2023.111031.

[20] Amaro AM, Reis PNB, Magalhães AG, de Moura MFSF. The influence of the boundary conditions on low-velocity impact composite damage. Strain 2011;47(s1):e220–6. http://dx.doi.org/10.1111/j.1475-1305.2008.00534.x.

[21] ASTM D7136/D7136M-05, standard test method for measuring the damage resistance of a fiber reinforced polymer matrix composite to a drop weight impact event. Am Soc Test Mater 2005.

[22] Reis PNB, Coelho CACP, Navalho FVP. Impact response of composite sandwich cylindrical shells. Appl Sci 2021;11(22). http://dx.doi.org/10.3390/app112210958.

[23] Coelho C, Navalho FP, Reis PNB. Impact response of laminated cylindrical shells. Frat Integr Strutt 2019;13:411–8. http://dx.doi.org/10.3221/IGF-ESIS.48.39.

[24] Ferreira LM, Coelho CACP, Reis PNB. Numerical simulations of the low-velocity impact response of semicylindrical woven composite shells. Materials 2023;16(9). http://dx.doi.org/10.3390/ma16093442.

[25] Ferreira LM, Coelho CACP, Reis PNB. Effect of cohesive properties on low-velocity impact simulations of woven composite shells. Appl Sci 2023;13(12):6948. http://dx.doi.org/10.3390/app13126948.

[26] Systemes D. ABAQUS. URL: https://www.3ds.com/products-services/simulia/products/abaqus/.

[27] User A. VUMAT for fabric reinforced composites. Dassault Systèmes; 2008.

[28] Johnson A, Pickett A, Rozycki P. Computational methods for predicting impact damage in composite structures. Compos Sci Technol 2001;61(15):2183–92. http://dx.doi.org/10.1016/S0266-3538(01)00111-7.

[29] Ladeveze P, LeDantec E. Damage modelling of the elementary ply for laminated composites. Compos Sci Technol 1992;43(3):257–67. http://dx.doi.org/10.1016/0266-3538(92)90097-M.

[30] Hou J, Ruiz C. Measurement of the properties of woven CFRP T300/914 at different strain rates. Compos Sci Technol 2000;60(15):2829–34. http://dx.doi.org/10.1016/S0266-3538(00)00151-2.

[31] Donadon MV, de Almeida SFM. Intralaminar fracture toughness characterization of composite laminates. In: Těšinova P, editor. Advances in composite materials. Rijeka: IntechOpen; 2011, http://dx.doi.org/10.5772/17156.

[32] Donadon MV, Falzon BG, Iannucci L, Hodgkinson JM. Intralaminar toughness characterisation of unbalanced hybrid plain weave laminates. Composites A 2007;38(6):1597–611. http://dx.doi.org/10.1016/j.compositesa.2006.12.003.

[33] Daudeville L, Allix O, Ladevèze P. Delamination analysis by damage mechanics: Some applications. Compos Eng 1995;5(1):17–24. http://dx.doi.org/10.1016/0961-9526(95)93976-3.

[34] Zou Z, Reid S, Li S. A continuum damage model for delaminations in laminated composites. J Mech Phys Solids 2003;51(2):333–56. http://dx.doi.org/10.1016/S0022-5096(02)00075-3.

[35] Camanho PP, Davila CG, de Moura MF. Numerical simulation of mixed-mode progressive delamination in composite materials. J Compos Mater 2003;37(16):1415–38. http://dx.doi.org/10.1177/0021998303034505.

[36] Turon A, Dávila C, Camanho P, Costa J. An engineering solution for mesh size effects in the simulation of delamination using cohesive zone models. Eng Fract Mech 2007;74(10):1665–82. http://dx.doi.org/10.1016/j.engfracmech.2006.08.025.

[37] Song K, Dávila CG, Rose CA. Guidelines and parameter selection for the simulation of progressive delamination. Vol. 41, 2008, p. 43–4.

[38] Nguyen K-H, Ju H-W, Truong V-H, Kweon J-H. Delamination analysis of multi-angle composite curved beams using an out-of-autoclave material. Compos Struct 2018;183:320–30. http://dx.doi.org/10.1016/j.compstruct.2017.03.078.

[39] Benzeggagh M, Kenane M. Measurement of mixed-mode delamination fracture toughness of unidirectional glass/epoxy composites with mixed-mode bending apparatus. Compos Sci Technol 1996;56(4):439–49. http://dx.doi.org/10.1016/0266-3538(96)00005-X.

[40] Campillo R, Moura D, Gonçalves D, da Silva J, Banea M, da Silva L. Fracture toughness determination of adhesive and co-cured joints in natural fibre composites. Composites B 2013;50:120–6. http://dx.doi.org/10.1016/j.compositesb.2013.01.025.

[41] Davies P, Sargent J. In: Blackman B, Pavan A, Williams J, editors. Fracture mechanics tests to characterize bonded glass/epoxy composites: application to strength prediction in structural assemblies. European structural integrity society, vol. 32, Elsevier; 2003, p. 279–92. http://dx.doi.org/10.1016/S1566-1369(03)80102-4.

[42] Heimbs S, Bergmann T, Schueler D, Toso-Pentecôte N. High velocity impact on preloaded composite plates. Compos Struct 2014;111:158–68. http://dx.doi.org/10.1016/j.compstruct.2013.12.031.

[43] Kinvi-Dossou G, Matadi Boumbimba R, Bonfoh N, Koutsawa Y, Eccli D, Gerard P. A numerical homogenization of E-glass/acrylic woven composite laminates: Application to low velocity impact. Compos Struct 2018;200:540–54. http://dx.doi.org/10.1016/j.compstruct.2018.05.137.

[44] Völkerink O, Koord J, Petersen E, Hühne C. Comparison of continuum shell and solid element-based modeling strategies for mesoscale progressive damage analysis of fiber composites. Mech Compos Mater 2023;59:2019–238. http://dx.doi.org/10.1007/s11029-023-10093-y.

[45] Batra R, Gopinath G, Zheng J. Damage and failure in low energy impact of fiber-reinforced polymeric composite laminates. Compos Struct 2012;94(2):540–7. http://dx.doi.org/10.1016/j.compstruct.2011.08.015.

[46] Schön J. Coefficient of friction of composite delamination surfaces. Wear 2000;237(1):77–89. http://dx.doi.org/10.1016/S0043-1648(99)00315-4.

[47] Bresciani L, Manes A, Ruggiero A, Iannitti G, Giglio M. Experimental tests and numerical modelling of ballistic impacts against Kevlar 29 plain-woven fabrics with an epoxy matrix: Macro-homogeneous and Meso-heterogeneous approaches. Composites B 2016;88:114–30. http://dx.doi.org/10.1016/j.compositesb.2015.10.039.

[48] Lopes C, Camanho P, Gürdal Z, Maimí P, González E. Low-velocity impact damage on dispersed stacking sequence laminates. Part II: Numerical simulations. Compos Sci Technol 2009;69(7):937–47. http://dx.doi.org/10.1016/j.compscitech.2009.02.015.

[49] Hameed MA, Ibrahim GR, Albarbar A. Effect of friction and shear strength enhancement on delamination prediction. J Compos Mater 2020;54(23):3329–42. http://dx.doi.org/10.1177/0021998320911719.

[50] Avila AF, Soares MI, Silva Neto A. A study on nanostructured laminated plates behavior under low-velocity impact loadings. Int J Impact Eng 2007;34(1):28–41. http://dx.doi.org/10.1016/j.ijimpeng.2006.06.009, International Conference on Impact Loading of Lightweight Structures.

[51] Ferreira L, Coelho C, Reis P. Impact response of semi-cylindrical composite laminate shells under repeated low-velocity impacts. In: 2022 advances in science and engineering technology international conferences. ASET, 2022, p. 1–5. http://dx.doi.org/10.1109/ASET53988.2022.9735043.

[52] Reis P, Ferreira J, Santos P, Richardson M, Santos J. Impact response of Kevlar composites with filled epoxy matrix. Compos Struct 2012;94(12):3520–8. http://dx.doi.org/10.1016/j.compstruct.2012.05.025.

[53] Schoeppner GA, Abrate S. Delamination threshold loads for low velocity impact on composite laminates. Compos A 2000;31(9):903–15. http://dx.doi.org/10.1016/S1359-835X(00)00061-0.

[54] Belingardi G, Vadori R. Low velocity impact tests of laminate glass-fiber-epoxy matrix composite material plates. Int J Impact Eng 2002;27(2):213–29. http://dx.doi.org/10.1016/S0734-743X(01)00040-9.

[55] Jones RM. Mechanics of composite materials. CRC Press; 2018.

[56] David-West O, Nash D, Banks W. An experimental study of damage accumulation in balanced CFRP laminates due to repeated impact. Compos Struct 2008;83(3):247–58. http://dx.doi.org/10.1016/j.compstruct.2007.04.015.

[57] Kistler L. Experimental investigation of the impact response of cylindrically curved laminated composite panels. In: 35th Structures, Structural Dynamics, and Materials Conference, Hilton Head, SC, U.S.A.. 1994, p. 1604. http://dx.doi.org/10.2514/6.1994-1604.

[58] Wu Z, Huang L, Pan Z, Zhang B, Hu X. Effect of off-axial angle on the low-velocity impact performance of braided laminates. Int J Mech Sci 2022;216:106967. http://dx.doi.org/10.1016/j.ijmecsci.2021.106967.

[59] Zhang D, Gu Y, Zhang Z, Jia M, Yue S, Li G. Effect of off-axis angle on low-velocity impact and compression after impact damage mechanisms of 3D woven composites. Mater Des 2020;192:108672. http://dx.doi.org/10.1016/j.matdes.2020.108672.

[60] Amaro AM, Reis PNB, de Moura M, Santos JB. Influence of the specimen thickness on low velocity impact behavior of composites. J Polym Eng 2012;32(1). http://dx.doi.org/10.1515/polyeng-2011-0101.

[61] Giancaspro JW, Papakonstantinou CG, Balaguru PN. Flexural response of inorganic hybrid composites with E-glass and carbon fibers. J Eng Mater Technol 2010;132(2):021005. http://dx.doi.org/10.1115/1.4000670.